Atmospheric turbulence profiling with a Shack-Hartmann wavefront sensor

Ogane, Hajime, Akiyama, Masayuki, Oya, Shin, Ono, Yoshito

Hajime Ogane, Masayuki Akiyama, Shin Oya, Yoshito Ono, "Atmospheric turbulence profiling with a Shack-Hartmann wavefront sensor," Proc. SPIE 11448, Adaptive Optics Systems VII, 114487P (13 December 2020); doi: 10.1117/12.2562320

SPIE.

Event: SPIE Astronomical Telescopes + Instrumentation, 2020, Online Only

Atmospheric turbulence profiling with a Shack-Hartmann wavefront sensor

Hajime Ogane[a], Masayuki Akiyama[a], Shin Oya[b], and Yoshito Ono[c]

[a]Astronomical Institute, Tohoku University, 6-3 Aramaki, Aoba-ku Sendai, Miyagi 980-8578, Japan
[b]National Astronomical Observatory of Japan, 2-21-1 Osawa, Mitaka, Tokyo 181-8588, Japan
[c]Subaru Telescope, National Astronomical Observatory of Japan, 650 North Aohoku Place Hilo, HI 96720, USA

ABSTRACT

In order to measure the altitude profile of the atmospheric turbulence in real-time, we are applying a MASS-DIMM method (Multi Aperture Scintillation Sensor and Differential Image Motion Monitor) to the Shack-Hartmann wavefront sensor data. Tomographic estimation of the atmospheric turbulence is a key technique in new generation of adaptive optics systems with multiple guide stars, and the real-time turbulence profiling provide a useful prior information for the tomography, which is an ill-posed inverse problem. By using the data of a Shack-Hartmann sensor, a turbulence profile in the same direction as the AO correction can be acquired. Moreover, since more information can be used compared with the traditional MASS-DIMM, the resolution in the height direction can be increased. This time, the data of the Shack-Hartmann sensor attached to Tohoku University 50cm telescope was analyzed, and the estimation of the turbulence profile was obtained. Similar profiles were obtained while the elevation of the star and the apparent distance to the turbulence changed in one hour monitoring measurements. The results supported the validity of the method.

Keywords: atmospheric turbulence, scintillation, Shack-Hartmann wavefront sensor, adaptive optics

1. INTRODUCTION

In the last decade, adaptive optics (AO) systems using multiple laser guide stars (LGSs) and wavefront sensors (WFSs) have been demonstrated or developed for 8m-class telescopes.[1–5] These systems measure the wavefront distortion in several lines of sight and reconstruct the distortions optimized in the direction of science objects using tomographic estimation. The tomographic estimation of the three-dimensional turbulence structure requires prior information of the turbulence strength as a function of altitude, which is called atmospheric turbulence profile. Because atmospheric condition varies with time, turbulence profile should be updated in a timescale of tens of minutes, which is the typical time scale of the profile time evolution.[6,7]

A number of methods to obtain real-time atmospheric turbulence profile based on optical triangulation have been developed.[8–10] However, these triangulation-based methods do not have any sensitivity to turbulence at high altitudes since spatial correlation length created by high turbulence layer is larger than the size of the pupil. Multi aperture scintillation sensor and differential image motion monitor (MASS-DIMM[11]) is one of the most common profilers, which uses a single star and has lower altitude resolution compared to the triangulation-based methods.

In this article, we propose a new turbulence profiling method, which carries out scintillation measurement similar to MASS using spot brightness fluctuation data of Shack-Hartmann wavefront sensor (SH-WFS). This new method, SH-MASS can measure the scintillation with more spacial patterns than the traditional MASS instrument, and makes it possible to profile the atmospheric turbulence with high altitude resolution by the observation of scintillation of a single star.

Further author information: (Send correspondence to H.O.)
H.O.: E-mail: h.ogane@astr.tohoku.ac.jp

Adaptive Optics Systems VII, edited by Laura Schreiber, Dirk Schmidt, Elise Vernet, Proc. of SPIE
Vol. 11448, 114487P · © 2020 SPIE · CCC code: 0277-786X/20/$21 · doi: 10.1117/12.2562320

2. PRINCIPLE

2.1 Brief review of the principle of MASS

The principle is summarized following Kornilov et al. 2003[12] and Tokovinin et al. 2003.[13] Let us consider that light with a wavelength of λ passes through atmospheric turbulence layers whose altitude is h_i, thickness is Δh_i, and strength is $C_N^2(h_i)$. Assuming the Kolmogorov's turbulence model, the Fresnel propagation, and the weak perturbation approximation, the spatial power spectrum of the intensity fluctuation $\Phi_I[\mathrm{m}^2]$ is written as follows,

$$\Phi_I(f_x, f_y) = \sum_i^{N_{\mathrm{layer}}} 1.53 f^{-11/3} \left\{ \frac{\sin(\pi\lambda h_i f^2)}{\lambda} \right\}^2 C_N^2(h_i)\Delta h_i, \tag{1}$$

where f_x, f_y are spatial frequencies and $f = \sqrt{f_x^2 + f_y^2}$. N_{layer} is the number of atmospheric turbulence layers. This expression means that the power of scintillation has its peak at the spatial frequency of $f \sim (\lambda h_i)^{-1/2}$ for each layer. Hence, detecting scintillation at different spatial frequencies makes it possible to discern the contributions from turbulence layers at different altitudes.

MASS instrument divides the pupil into several concentric annuli and measures the starlight intensity in the concentric apertures. The intensity fluctuation is characterized with the scintillation index (SI), which is the variance and covariance of the normalized intensity observed by the concentric apertures. Denoting the observed intensity in the X-th annulus as I_X, the intensity variance of the X-th annulus, referred as normal scintillation index, is defined as follows,

$$s_X = \mathrm{Var}\left[\frac{I_X}{\langle I_X \rangle} \right], \tag{2}$$

where $\langle\rangle$ represents time-average, and Var means variance. Likewise, the intensity covariance of the X-th and Y-th annuli, referred as a differential scintillation index, is defined as

$$s_{XY} = \mathrm{Var}\left[\frac{I_X}{\langle I_X \rangle} - \frac{I_Y}{\langle I_Y \rangle} \right] = s_X + s_Y - 2\mathrm{Cov}\left[\frac{I_X}{\langle I_X \rangle}, \frac{I_Y}{\langle I_Y \rangle} \right], \tag{3}$$

where Cov means covariance. These SIs can be expressed using the power spectrum of intensity fluctuation $\Phi_I(f_x, f_y)$ as follows,

$$s_X = \iint \Phi_I(f_x, f_y) |\mathcal{F}[A_X(x,y)]|^2 df_x df_y, \tag{4}$$

$$s_{XY} = \iint \Phi_I(f_x, f_y) |\mathcal{F}[A_X(x,y) - A_Y(x,y)]|^2 df_x df_y, \tag{5}$$

where $\mathcal{F}$ means Fourier transformation and $A(x,y)$ is the normalized aperture function; a function which returns value of 1 divided by the area of the aperture for (x,y) inside the aperture and value of 0 for others. Using Eq.1 into $\Phi_I(f_x, f_y)$ in Eq.4 and Eq.5, following equations are obtained.

$$s_X = \sum_i^{N_{\mathrm{layer}}} W_{X,i} J_i, \tag{6}$$

$$s_{XY} = \sum_i^{N_{\mathrm{layer}}} W_{XY,i} J_i, \tag{7}$$

where

$$W_{X,i} = \iint 1.53 f^{-11/3} \left\{ \frac{\sin(\pi\lambda h_i f^2)}{\lambda} \right\}^2 |\mathcal{F}[A_X(x,y)]|^2 df_x df_y, \tag{8}$$

$$W_{XY,i} = \iint 1.53 f^{-11/3} \left\{ \frac{\sin(\pi\lambda h_i f^2)}{\lambda} \right\}^2 |\mathcal{F}[A_X(x,y) - A_Y(x,y)]|^2 df_x df_y. \tag{9}$$

$$J_i = C_N^2(h_i)\Delta h_i. \tag{10}$$

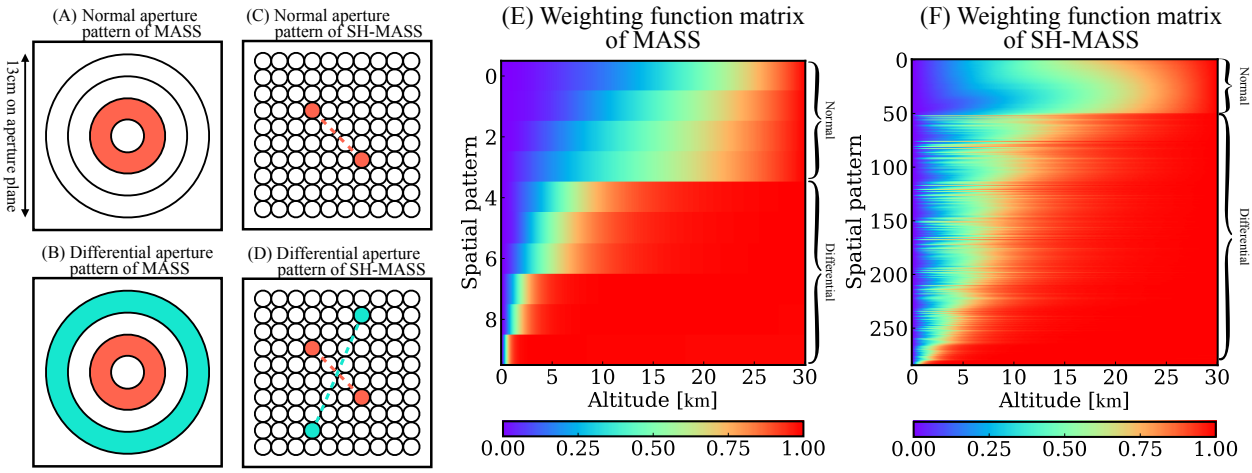

Figure 1. (A) An example of MASS spatial pattern (red annulus) whose measurement is used to compute normal SI. (B) An example of MASS spatial patterns (red and blue annuli) whose measurements are used to compute differential SI. (C) An example of SH-MASS spatial pattern (red subaperture pair) whose measurement is used to compute normal SI. (D) An example of SH-MASS spatial patterns (red and blue subaperture pairs) whose measurements are used to compute differential SI. In the calculation of differential SIs, only two subaperture pairs which have common mid point are used. Each pixel is coloured with weight value [$\mathrm{m}^{-1/3}$] normalized in each row so that characteristic altitude where weight value reaches 50%-ile can be seen as light green. (E) WF matrix of the traditional MASS. (F) WF matrix of the SH-MASS

$W_{X,i}$ and $W_{XY,i}$ are called normal weighting functions (WFs) and differential WFs, respectively, which can be calculated from the information of aperture geometry and measurement wavelength. By solving Eq.6 and Eq.7, turbulence strengths $J_i = C_N^2(h_i)\Delta h_i$ of multiple layers are estimated.

2.2 Application of SH-WFS data to MASS

Panels A, B, C, and D in Fig.1 show comparison of the definition of spatial patterns in traditional MASS (A and B) and SH-MASS (C and D). In traditional MASS case, concentric annular spatial patterns which have the diameters of 2.0, 3.7, 7.0, and 13.0 cm are used in order to extract scintillation at a specific frequency which corresponds to each of the diameters.

On the other hand, we define a subaperture pair, which consists of two subapertures, as one spatial pattern of SH-MASS so that we can effectively extract a certain spatial frequency component of scintillation which is characterized by the distance of the two subapertures. Then, total intensity of a subaperture pair is used as a measured value to calculate a SI. Based on this definition of normal SI, Eq.2 can be rewritten as,

$$\begin{aligned} s_X &= \mathrm{Var}\left[\frac{I_X}{\langle I_X\rangle}\right] \\ &= \mathrm{Var}\left[\frac{I_i + I_j}{\langle I_i + I_j\rangle}\right] \\ &= \frac{\mathrm{Var}[I_i] + \mathrm{Var}[I_j] + 2\mathrm{Cov}[I_i, I_j]}{(\langle I_i\rangle + \langle I_j\rangle)^2}, \end{aligned} \tag{11}$$

where i, j are indices of subapertures which constitutes aperture X, and I_i represents spot intensity (or counts) observed in i-th subaperture. Thanks to a large number of SH-WFS subapertures, there are many subaperture pairs which have common separation distance. Then, we calculated normal SIs for all subaperture pairs which have a common spatial distance and regarded average and standard deviation as a normal SI and its measurement error, respectively.

Likewise, a differential SI is defined as a fluctuation covariance between total intensity measured by the two

subaperture pairs. Then, Eq.3 can be rewritten as,

$$\begin{aligned} s_{XY} &= s_X + s_Y - 2\mathrm{Cov}\left[\frac{I_X}{\langle I_X\rangle}, \frac{I_Y}{\langle I_Y\rangle}\right] \\ &= s_X + s_Y - 2\mathrm{Cov}\left[\frac{I_i + I_j}{\langle I_i + I_j\rangle}, \frac{I_k + I_l}{\langle I_k + I_l\rangle}\right] \\ &= s_X + s_Y - 2\frac{\mathrm{Cov}[I_i, I_k] + \mathrm{Cov}[I_j, I_k] + \mathrm{Cov}[I_i, I_l] + \mathrm{Cov}[I_j, I_l]}{(\langle I_i\rangle + \langle I_j\rangle)(\langle I_k\rangle + \langle I_l\rangle)} \end{aligned} \tag{12}$$

where i, j are indices of subapertures which constitutes aperture X, while k, l means indices of subapertures for aperture Y. Here, we calculated differential SIs for two subaperture pairs which have common mid point. That corresponds to taking concentric two annuli in the traditional MASS. By these definitions of spatial patterns in SH-MASS, 51 normal SIs and 234 differential SIs are obtained with 10×10 SH-WFS.

Panels E and F in Fig.1 shows the comparison of WFs of the traditional MASS and SH-MASS which are calculated assuming the aperture geometries shown in panels A-D and measurement wavelength of 500 nm. Each row of the WF matrix represents WF of each spatial pattern, i.e. Eq.8 or Eq.9. Here, values of WFs are normalized in each row so that the transition of weight value in altitude direction can be easily recognized. While the traditional MASS WF has a small number of spatial patterns with a discontinuity at $\sim$ 10km, in SH-MASS case, the number of spatial patterns reaches $\sim$ 300 and their transition altitudes are continuous from the ground to 20 km high, which implies SH-MASS's aperture geometry gives sufficient number of constraints to estimate a turbulence profile with higher altitude resolution.

2.3 Profile reconstruction method

Reconstruction of a turbulence profile is solving an inverse problem described as Eq.6 and Eq.7 with analytically-derived WF matrix. If we simply apply a linear reconstruction without consideration of the parameter range, negative turbulence strength often appears. In order to avoid the situation, in this study, the turbulence profile and associated uncertainty are evaluated based on Bayesian inference with Marcov Chain Monte Carlo (MCMC) method. As a prior function of MCMC, we applied top-hat filter to limit the parameter space as follows,

$$P(\vec{J}) = \begin{cases} 1 & \text{if } -32 < \log J_i[\mathrm{m}^{1/3}] < -11 \text{ is satisfied by all } J_i, \\ 0 & \text{otherwise,} \end{cases} \tag{13}$$

where $\vec{J}$ is the turbulence profile. The strength range of each turbulence layer i.e. $-32 < \log J_i[\mathrm{m}^{1/3}] < -11$ corresponds to $2.0 \times 10^{-2} < r_0[\mathrm{m}] < 8.0 \times 10^{10}$ in the Fried parameter assuming measurement wavelength of 500 nm and zenith direction. It is expected that this parameter range covers the possible turbulence strength of a single layer. As a likelihood function of MCMC, we use the probability that the observed SIs are obtained from a Gaussian distribution with a mean of the expected SIs and a standard deviation of observation errors as follows,

$$L(\vec{s}|\vec{J}) = \prod_{m=1}^{M} \left(\frac{1}{\sqrt{2\pi\sigma_m^2}} \exp\left[-\frac{(s_m - (W\vec{J})_m)^2}{2\sigma_m^2} \right] \right), \tag{14}$$

where M is the number of spatial patterns, $\vec{s}$ and $\vec{\sigma}$ are SIs and their errors, respectively, W is WF matrix, and $\vec{J}$ is the turbulence profile. The reconstruction procedure was conducted utilizing *emcee*, a MCMC tool for *Python*.

3. PERFORMANCE EVALUATION

In order to investigate the SH-MASS's performance quantitatively, we calculate the response of SH-MASS to a single turbulence layer. At first, we create a turbulence profile which consists of single turbulence layer at a certain altitude. Next, we calculate theoretical SIs by multiplying WF to the turbulence profile assuming the measured wavelength of 500 nm. Finally, turbulence profile is reconstructed for a predefined set of layers by

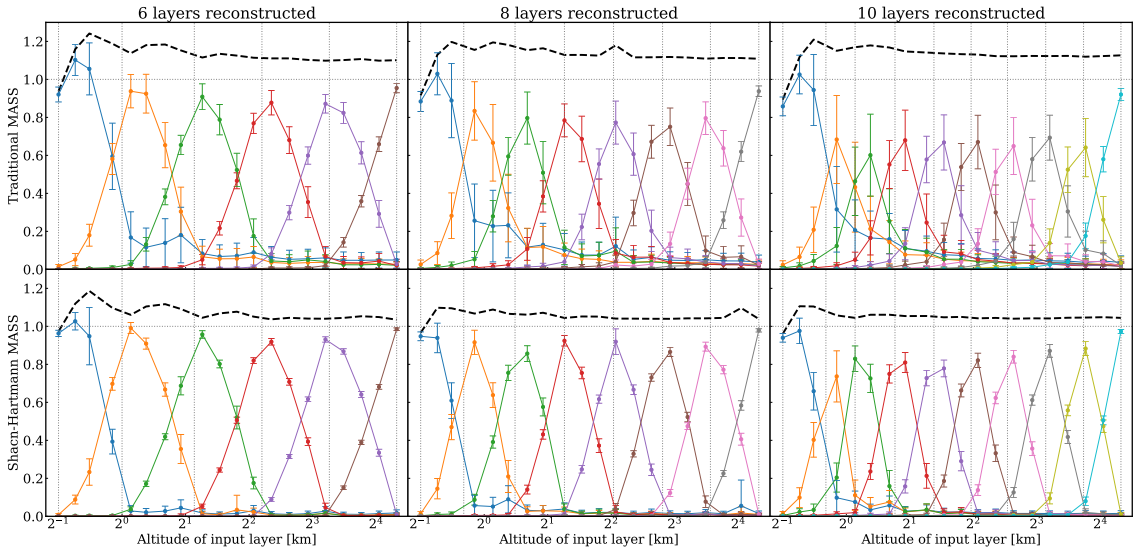

Figure 2. Top panels: The response function for the traditional MASS setup in which turbulence strengths of 6, 8, and 10 layers are reconstructed using scintillation data observed by 4 concentric annular apertures. Bottom panels: The response function for classical SH-MASS setup in which turbulence strengths of 6, 8, and 10 layers are reconstructed using scintillation data observed by 10x10 SH-WFS whose subaperture diameter corresponds to 1.3 cm on the primary mirror. In each panels, each line represents the response of each reconstruction layer to the input single turbulence layer. In the cases of 6, 8, and 10 layers are reconstructed, the altitudes of the reconstruction layers are [0.5, 1.0, 2.2, 4.6, 9.6, 20.0] km, [0.5, 0.8, 1.4, 2.4, 4.1, 7.0, 11.8, 20.0] km, and [0.5, 0.8, 1.1, 1.7, 2.6, 3.9, 5.8, 8.8, 13.3, 20.0] km, respectively. Black dashed line represents the total sensitivity as a sum of the response of all the reconstruction layers. Gray vertical lines stand for the altitude of reconstructed layers, while gray horizontal line stands for the sensitivity when all input turbulence strength are sensed.

using the MCMC method described in the last section. Here, we assume that measurement errors of SIs are 5% of SIs uniformly for all spatial patterns. Because errors of SIs are typically approximately 2% except for 3-7% error for the smallest differential SI,[13] our assumption of 5% errors would be suitable in order to explore the worst case of typical performance of SH-MASS. We repeat this procedure with changing the altitude of input single turbulence layer to obtain a response function, which is defined as estimated turbulence strength of each reconstructed layer as a function of altitude of the input single turbulence layer.

In Fig.2, the response function of the traditional MASS (top panels) and that of SH-MASS (bottom panels) are compared. The assumed spatial pattern for both of the MASS and SH-MASS are same as Fig.1. Each colored line represents the sensitivity of each reconstructed layer, and errors are defined as the standard deviation of solutions from 10000 MCMC steps after convergence. By comparing the top panels with bottom panels, it is clear that the estimation errors are smaller in SH-MASS. In addition, the high estimation accuracy of SH-MASS is kept even when ten layers are reconstructed. The black dashed lines are also closer to unity in SH-MASS cases, which means that the estimation of integrated turbulence strength is improved. These results indicate that a large number of spatial patterns realized by SH-WFS subaperture geometry is effective in reconstructing turbulence profiles with high altitude resolution and sufficient accuracy.

Fig.3 show how the shape of response function changes if parameters of SH-WFS are changed. The size of subaperture is varied in the left six panels, while the format of SH-WFS is varied in the right six panels. If the size of subaperture is increased, fine spatial structure of scintillation is no longer detectable. Then, scintillation measurement does not have any information of turbulence at low altitude which is associated with high spatial frequency scintillation pattern. Therefore, setting reconstructed layers at low altitude causes poor fitting. For this reason, the altitude of lowest reconstructed layer is changed so that the lowest altitude h_1 and the size of subaperture x_{subap} satisfy $x_{\mathrm{subap}} \sim \sqrt{\lambda h_1}$. Though SH-MASS with small subapertures makes it possible to estimate atmospheric turbulence down to close to the ground, small subaperture can be suffered from the problem of small number of photons. The diameter of subaperture should be determined carefully considering

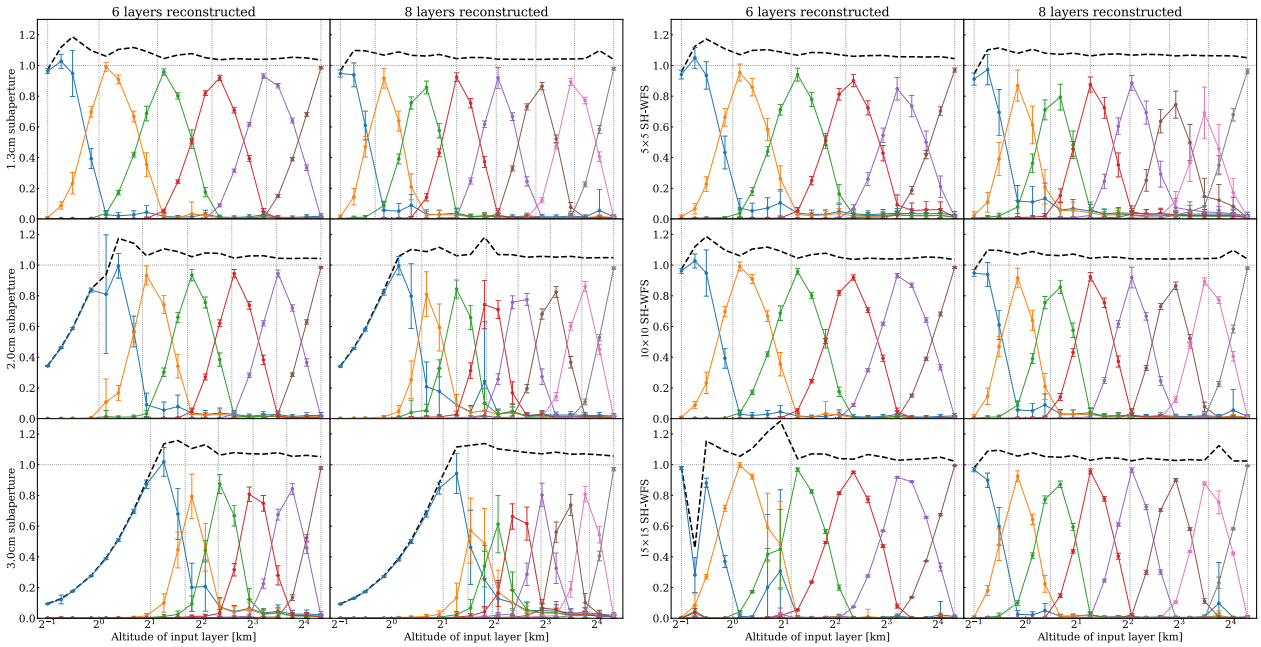

Figure 3. Response functions of SH-MASS with various SH-WFS parameters. Left: Subaperture diameter is changed to 1.3 cm (top), 2.0 cm (middle), and 3.0 cm (bottom). Here, format of SH-WFS is fixed to 10×10. Right: SH-WFS format is changed to 5×5 (top), 10×10 (middle), and 15×15 (bottom). Here, the diameter of subaperture is fixed to 1.3 cm.

the altitude range of estimation, the magnitude of available star, or the availability of highly sensitive detector with high pixel read out rate such as an electron multiplying CCD (EM-CCD). If the format of SH-WFS is larger, it is clear that the size of error becomes smaller. This is because of large number of constraints realized by larger format. The number of constraints is 43, 285, and 1740 for 5×5, 10×10, and 15×15 SH-WFS, respectively. On the other hand, in 15×15 case, MCMC solver does not converge well in some calculations. This would be because too many constraints result in complicated posterior probability distribution and causes poor convergence in Monte Carlo sampling. Considering the results and computational cost, the format of 10×10 is suitable size of SH-WFS.

4. ON-SKY EXPERIMENT

4.1 Setup and observation

In order to demonstrate the SH-MASS, we conducted a scintillation measurement using a wavefront sensor system attached to the 50 cm telescope, IK-51FC in Tohoku University. Our SH-WFS system is consist of a collimator, a Bessel's R band filter, a 150 μm pitch lenslet array (Thorlabs, MLA150-5C), relay lenses and an EMCCD camera with E2V CCD60 128×128 24 μm pixel detector and custom made readout electronics provided by Nuvu Cameras. The primary mirror of 50 cm telescope is effectively divided into 20×20 by the lenslet array. One pixel of the detector corresponds to 4.9 arcsec on the sky. Amplification signal of 42.6 V is applied to achieve factor 300 multiplication gain of the EMCCD. High speed imaging of 500Hz was repeated 30000 times targeting Deneb ($m_R = 1.14$[mag]). This procedure was repeated nine times in one hour on a clear night, October 16th, 2019 in Japan Standard Time. In the one hour, the elevation of the star changed from 46° to 34°.

4.2 Data analysis

First of all, the spot reference frame is created by averaging the 30000 frames in each dataset, and spot size and locations of spots are measured. By fitting each spot of the reference frame with a Gaussian function, the diameter of Airy disk is measured to be 4.45 pixels (FWHM is 1.88 pixels). We define region inside a circle with

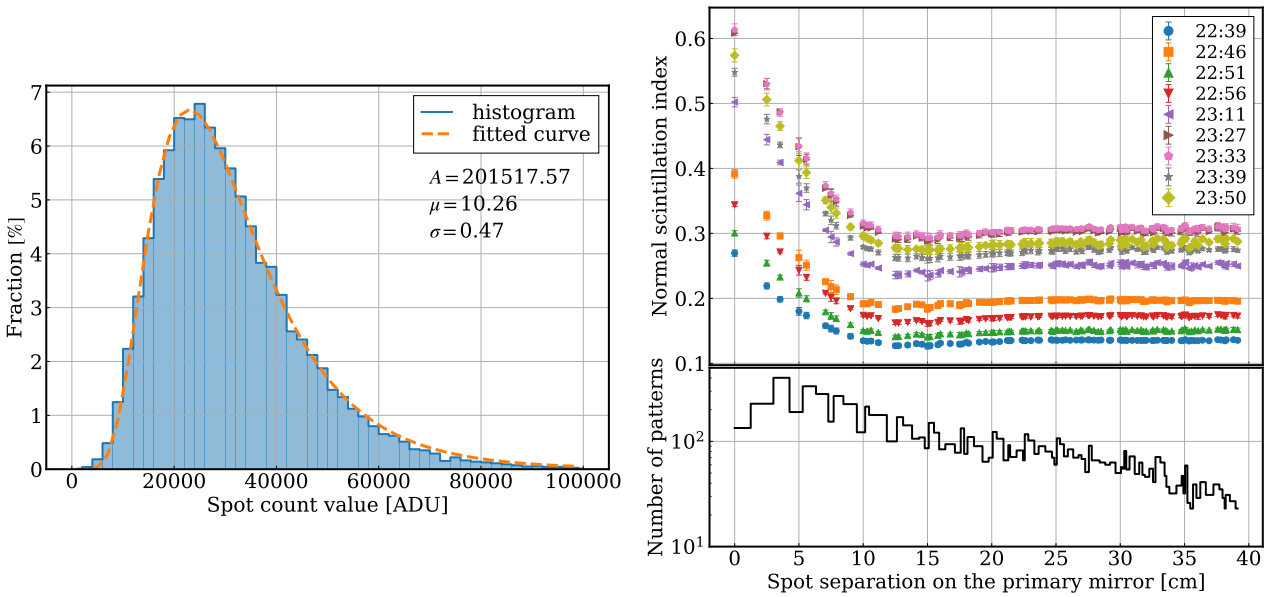

Figure 4. Left: Histogram of count values of one spot of SH-WFS measured with 500 Hz in 1 minute. The distribution is well fitted by a log-normal distribution, which implies that the detected intensity fluctuation is coming from scintillation. Right top: Observed normal SIs plotted as a function of a separation distance of two subapertures which constitutes the normal spatial pattern. Different colour represents different observation time. The SI value decreases and become flattened as the separation increases, which indicates that the typical correlation length of scintillation is shorter than 15 cm. And the trend that SIs become larger as time goes by can be explained by variation of the elevation angle of the star Right bottom: Histogram of the number of subaperture pairs which have common separation distance. The normal SIs and their errors in right-top figure have been calculated as the mean and standard deviation of these number of statistics.

a diameter of 5.0 pixels to measure its flux and outside of that region is used to estimate the sky background flux. Then, sky-subtracted spot counts are calculated for all the spots in the 30000 frames.

The distribution of light intensity induced by scintillation follows log-normal distribution[14] written as follows.

$$f(x) = \frac{A}{\sqrt{2\pi}\sigma x}\exp\left(\frac{(\ln x - \mu)^2}{2\sigma^2}\right), \tag{15}$$

where μ and σ are shape parameters of the distribution and A is a normalization parameter.

Then we check if measured count value follows this distribution. Left panel of Fig.4 shows the histogram of count values of one spot in one minute. The histogram is well fitted by a log-normal distribution function with parameters of $A = 2.0 \times 10^5$, $\mu = 10.26$ and $\sigma = 0.47$. All other spots also follow log-normal distribution, which supports that the observed intensity fluctuation of SH-WFS spots are caused by atmospheric turbulence. Next, SIs of all the spatial patterns are calculated from the count fluctuations of spots. The mean, variance and covariance of each spot's count fluctuation are computed and SIs are calculated following Eq.11 and Eq.12.

Finally, effects from finite exposure time are corrected. In this study, we follow the method described in Tokovinin et al.(2003),[13] in which ideal 0 millisecond SIs s_0 are estimated from linear extrapolation of SIs measured by τ milliseconds exposure s_τ and that measured by 2τ milliseconds exposure $s_{2\tau}$,

$$s_0 = 2s_\tau - s_{2\tau}. \tag{16}$$

Here, datasets with 2τ milliseconds exposure is effectively obtained by averaging two adjacent images in the data of τ milliseconds exposure.

Right-top panel of Fig.4 shows the observed normal SIs as a function of separation of two subapertures which constitutes a normal spatial pattern. Right-bottom panel of Fig.4 shows the number of subaperture pairs

which have common spatial pattern. At all observation time, the normal SI decreases as a function of subaperture separation and get flattened at spatial length of 10-15 cm and longer, which indicates that there are no turbulence higher than 20 km. The spatial scale of is consistent with the typical spatial scale of scintillation i.e. $\sqrt{\lambda h} \sim 11$ cm with the assumption of $\lambda \sim 600$ nm and $h \sim 20$ km. In addition, this feature can be understood using Eq.11. For null separation case, $\mathrm{Cov}[I_i, I_j]$ becomes $\mathrm{Var}[I_i]$, and SI becomes $\mathrm{Var}[I_i]/\langle I_i \rangle^2$. Whereas for very long separation case, $\mathrm{Cov}[I_i, I_j]$ becomes 0, and SI becomes $\mathrm{Var}[I_i]/2\langle I_i \rangle^2$, half of the SI for the null separation case. In Fig.4 actually, normal SIs for longer separation than 15 cm is almost half of normal SI for 0 cm separation. Besides, there is a trend that the value of SI become larger as time goes by. This can be explained by the change of the elevation of the star. As the elevation becomes lower, apparent altitude of turbulence layer becomes higher and apparent thickness of turbulence layer becomes thicker. Both effects account for the increase of SIs.

4.3 Atmospheric turbulence profile

Fig.5 shows the atmospheric turbulence profile reconstructed using the MCMC estimation method described in Sec.2.3. Different panel corresponds to different observation time. The reduced χ^2 values which are less than 10 in all datasets and the small uncertainties which represent one sigma values of turbulence strengths after MCMC convergence implies that the observed normal and differential SIs are described well with the scintillation model. In addition, the overall shape of the profiles shows that the strongest turbulence exists at the lowest layers and second strongest peak distributes at roughly 10 km. These profiles are consistent with that expected from the typical characteristics of the Earth's atmosphere such as the ground turbulent layer and the tropopause, respectively.

5. DISCUSSIONS

Although MCMC-based reconstruction method enables us to evaluate the turbulence profile including its estimation error, it requires large calculation cost. It typically takes a few tens of minutes for six-layer reconstruction with eight-core parallel processing using *Intel® Core™ i7-4790K* CPU and highly depends on the number of reconstructed layers. Atmospheric turbulence profile as a prior information for tomographic reconstruction matrix has to be updated in a timescale of tens of minutes. Therefore, we try faster profile calculation based on Broyden–Fletcher–Goldfarb–Shanno (BFGS) algorithm, which is one of iterative solvers for non-linear optimization problem. This algorithm can be utilized with *scipy.optimize.minimize* module for *Python*. We impose the same condition of $-32 < \log J_i[\mathrm{m}^{1/3}] < -11$ for all the component of $\vec{J}$ as MCMC-based method, and minimize the χ^2 function directly. However, in iterative calculation method, the solution is not necessarily the global minimum. Hence, we conduct the BFGS algorithm 1000 times from 1000 different random initial turbulence profile and pick out 100 final turbulence profiles whose χ^2 values are the smallest to calculate the mean and standard deviation of the 100 profiles.

In all observation time, both estimation methods reproduce the same turbulence profile. The consistency suggests that 1000-time iterative minimization from the random initial profiles is sufficient to find out the global minimum. Because the calculation time for the 1000-time iterative minimization is typically a few minutes, the iterative BFGS method can be used for a faster profile reconstruction. Then, we can conduct the profile estimation with 10 layers (1.0, 1.4, 1.9, 2.7, 3.8, 5.3, 7.4, 10.3, 14.3, 20.0 km), which takes the timescale of days when MCMC-based method is used. Here, higher altitude resolution with $dh/h = 1.4$ ($dh/h = 2.0$ for the traditional MASS) is realized for atmospheric turbulence which distributes from 1.0 km to 20.0 km. Precise understanding of turbulence distribution realized by the high altitude resolution is necessary to produce a realistic reconstruction matrix. For detailed information, refer a submitted paper "Atmospheric turbulence profiling with multi-aperture scintillation of a Shack-Hartmann sensor".

6. SUMMARY

In this study, we investigate a new MASS-based atmospheric turbulence profiling method called SH-MASS, which reproduces the profile from scintillation observed by a Shack-Hartmann wavefront sensor. Evaluating the response function of the SH-MASS in comparison with those of the traditional MASS makes it clear that SH-MASS theoretically has higher altitude resolution than traditional MASS under the assumption that the

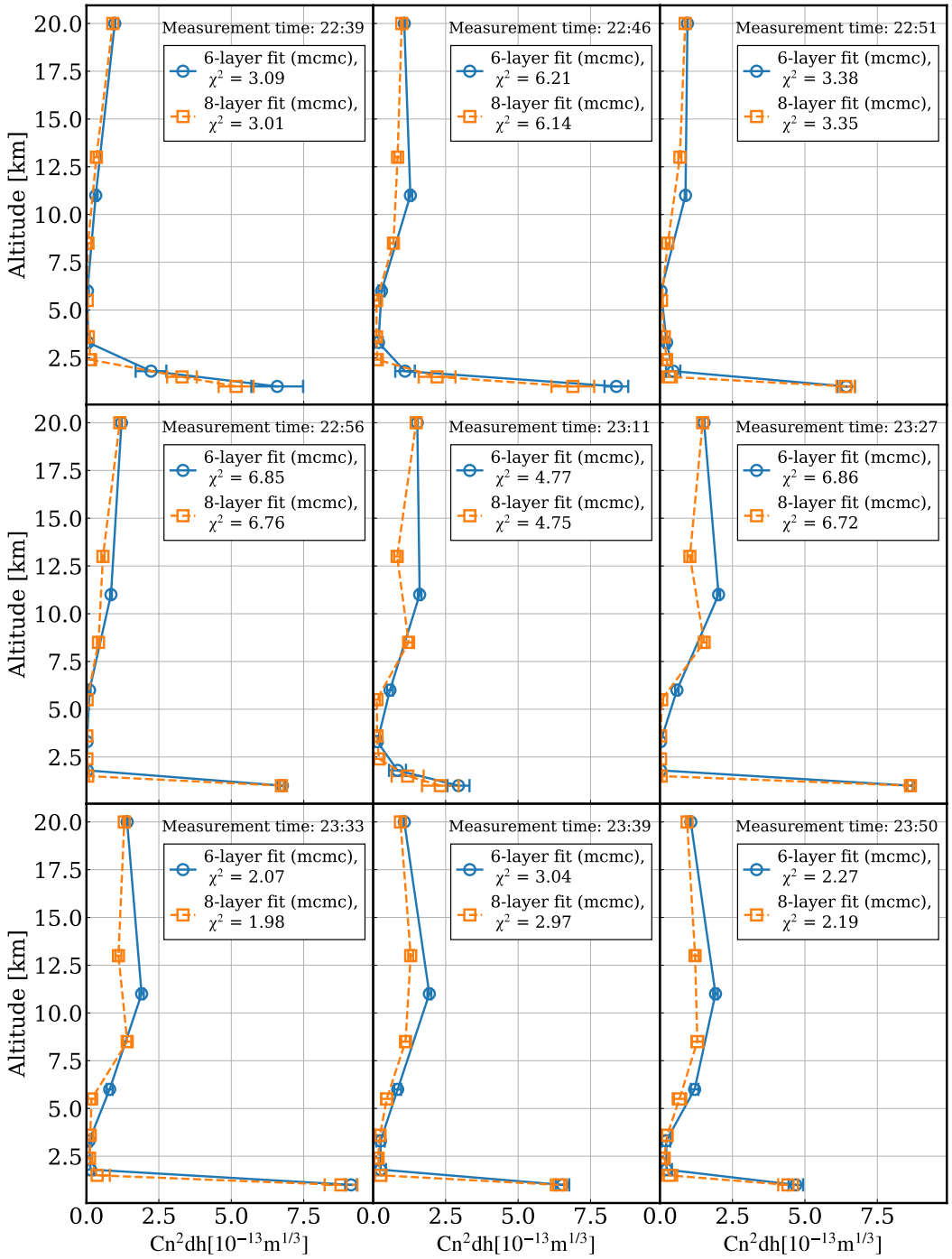

Figure 5. The atmospheric turbulence profile reonstructed by SIs measured at Tohoku university. These profiles are reconstructed by the MCMC estimation method mentioned in Sec.2.3. The effect of elevation angle of the star is corrected. Different panel corresponds to different observation time which is described in each panel's title. Blue lines are a profiles which are reconstructed assuming six layers while orange lines assume eight layers. Reduced χ^2 values of each profile estimation are shown in the legend.

scintillation measurements have 5% error. This high altitude resolution is enabled by a large number of spatial patterns realized by the grid pattern spots of SH-WFS.

By investigating the behaviour of response functions with changing the parameters of SH-MASS, it is confirmed that the smaller size of subaperture realizes higher sensitivity to the low altitude turbulence, and that the format of 10×10 is suitable considering the estimation error and the calculation convergence.

This new profiler is demonstrated with 50 cm telescope at Tohoku University and typical characteristics of the atmospheric turbulence are reproduced as the estimated turbulence profile. In order to decrease the calculation cost and meet the real time requirement of the profiling, i.e., one profile estimation per ~ 10 minutes, we confirm that faster iterative method can also reproduce the same profile as the MCMC-based method.

REFERENCES

[1] Marchetti, E., Brast, R., Delabre, B., Donaldson, R., Fedrigo, E., Frank, C., Hubin, N., Kolb, J., Lizon, J.-L., Marchesi, M., et al., "On-sky testing of the multi-conjugate adaptive optics demonstrator," *The Messenger* **129**(8) (2007).

[2] Arsenault, R., Madec, P.-Y., Paufique, J., La Penna, P., Stroebele, S., Vernet, E., Pirard, J.-F., Hackenberg, W., Kuntschner, H., Jochum, L., et al., "Eso adaptive optics facility progress report," in [*Adaptive Optics Systems III*], **8447**, 84470J, International Society for Optics and Photonics (2012).

[3] Lardière, O., Andersen, D., Blain, C., Bradley, C., Gamroth, D., Jackson, K., Lach, P., Nash, R., Venn, K., Véran, J.-P., et al., "Multi-object adaptive optics on-sky results with raven," in [*Adaptive Optics Systems IV*], **9148**, 91481G, International Society for Optics and Photonics (2014).

[4] Rigaut, F., Neichel, B., Boccas, M., d'Orgeville, C., Vidal, F., van Dam, M. A., Arriagada, G., Fesquet, V., Galvez, R. L., Gausachs, G., et al., "Gemini multiconjugate adaptive optics system review–i. design, trade-offs and integration," *Monthly Notices of the Royal Astronomical Society* **437**(3), 2361–2375 (2014).

[5] Minowa, Y., Clergeon, C., Akiyama, M., Rigaut, F., d'Orgeville, C., Price, I., Herrald, N., Koyama, Y., Iwata, I., Hattori, T., et al., "Ultimate-subaru: Wide-field near-infrared surveyor with glao at subaru telescope," *Adaptive Optics for Extremely Large Telescopes V (AO4ELT5)],(Jun 2017)* (2017).

[6] Gendron, E., Morel, C., Osborn, J., Martin, O., Gratadour, D., Vidal, F., Le Louarn, M., and Rousset, G., "Robustness of tomographic reconstructors versus real atmospheric profiles in the elt perspective," in [*Adaptive Optics Systems IV*], **9148**, 91484N, International Society for Optics and Photonics (2014).

[7] Farley, O., Osborn, J., Morris, T., Fusco, T., Neichel, B., Correia, C., and Wilson, R., "Limitations imposed by optical turbulence profile structure and evolution on tomographic reconstruction for the elt," *Monthly Notices of the Royal Astronomical Society* **494**(2), 2773–2784 (2020).

[8] Rocca, A., Roddier, F., and Vernin, J., "Detection of atmospheric turbulent layers by spatiotemporal and spatioangular correlation measurements of stellar-light scintillation," *JOSA* **64**(7), 1000–1004 (1974).

[9] Avila, R., Vernin, J., and Masciadri, E., "Whole atmospheric-turbulence profiling with generalized scidar," *Applied Optics* **36**(30), 7898–7905 (1997).

[10] Wilson, R. W., "Slodar: measuring optical turbulence altitude with a shack–hartmann wavefront sensor," *Monthly Notices of the Royal Astronomical Society* **337**(1), 103–108 (2002).

[11] Kornilov, V., Tokovinin, A., Shatsky, N., Voziakova, O., Potanin, S., and Safonov, B., "Combined mass–dimm instruments for atmospheric turbulence studies," *Monthly Notices of the Royal Astronomical Society* **382**(3), 1268–1278 (2007).

[12] Kornilov, V., Tokovinin, A. A., Vozyakova, O., Zaitsev, A., Shatsky, N., Potanin, S. F., and Sarazin, M. S., "Mass: a monitor of the vertical turbulence distribution," in [*Adaptive Optical System Technologies II*], **4839**, 837–845, International Society for Optics and Photonics (2003).

[13] Tokovinin, A., Kornilov, V., Shatsky, N., and Voziakova, O., "Restoration of turbulence profile from scintillation indices," *Monthly Notices of the Royal Astronomical Society* **343**(3), 891–899 (2003).

[14] Zhu, X. and Kahn, J. M., "Free-space optical communication through atmospheric turbulence channels," *IEEE Transactions on communications* **50**(8), 1293–1300 (2002).